IEEE Access
Multidisciplinary | Rapid Review | Open Access Journal

Received 12 July 2022, accepted 29 July 2022, date of publication 8 August 2022, date of current version 12 August 2022.

Digital Object Identifier 10.1109/ACCESS.2022.3197284

APPLIED RESEARCH

Implementation of a Controller for a Space-Grade, Piezo-Actuated Fabry-Perot Interferometer

CHRISTER HOLMLUND, (Member, IEEE), AND ROBERTS TROPS
VTT Technical Research Centre of Finland Ltd., 02150 Espoo, Finland

Corresponding author: Christer Holmlund (christer.holmlund@vtt.fi)

This work was supported by the VTT Technical Research Centre of Finland Ltd., within the Project "Development of a Fabry-Perot Assembly EQM for the ALTIUS Instrument; ALTIUS Instrument Pre-Development" funded by the European Space Agency (ESA) and carried out under direct contract with OIP Sensor Systems.

ABSTRACT A tunable Fabry-Perot interferometer (FPI) can be used as an optical band-pass filter. This type of filter is used in spectrometers and spectral imagers. The transmitted wavelength depends on the optical cavity adjusted by an electronic controller. This cavity, or the gap between the FPI mirrors, is measured using capacitive sensing. The performance of the FPI controller directly affects the FPI transmission spectrum and thus the quality of the spectral data. This work describes the design of the FPI controller for the ultraviolet channel of the ALTIUS hyperspectral imager. The ALTIUS mission is part of the Earth Watch program managed by the European Space Agency, ESA. This article presents a novel combination of building blocks to implement a low-noise, high-stability controller for piezo-actuated FPIs. Special care was taken to guarantee temperature stability and to minimize fluctuation of the FPI gap caused by the controller electronics. With the controller design presented in this paper, temperature variations ranging from –50 to +50 °C induce FPI gap deviations of less than 0.1 nm at an electrode distance of 3000 nm, corresponding to a relative temperature drift of 0.3 ppm/°C.

INDEX TERMS Aerospace electronics, analog circuits, capacitance measurement, capacitance-stabilized etalon, Fabry-Perot, feedback circuits, position measurement, pulse width modulation.

I. INTRODUCTION

This work was carried out during the pre-development phase of the Fabry-Perot interferometer assembly for the ultraviolet channel of the ALTIUS instrument. ALTIUS is an imaging spectrograph for the wavelength range from 250 to 1800 nm. ALTIUS is the primary payload of a spacecraft with the same name. The ALTIUS mission is part of the Earth Watch program managed by the European Space Agency, ESA [1], [2].

The UV channel of the ALTIUS instrument covers the wavelength range from 250 to 370 nm using a cascade of four Fabry-Perot interferometers. A Fabry-Perot interferometer (FPI) is an optical resonator consisting of two reflecting surfaces separated by some distance [3]. The distance between the reflecting surfaces determines the length of the optical resonator and the spectrum of the transmitted light. The relation between the wavelength λ, giving constructive interference, and the effective distance between the mirrors d is $\lambda = 2d/N$, where N is the order of interference. This expression holds for a light beam perpendicular to the mirrors. This tunable optical band-pass filter is used in spectrometers and spectral imagers.

By cascading FPIs and setting the individual mirror gaps to different, specific values, the operating wavelength range can be wider than achieved with a single FPI. However, to make this possible, the FPIs must be operated at low orders of interference, and thus, narrow mirror gaps. This condition, in turn, sets high requirements on the FPI controller, as gap variations directly affect the transmitted wavelength. Therefore, the mirror gap of the four FPIs must be continuously controlled

The associate editor coordinating the review of this manuscript and approving it for publication was Xi Zhu.

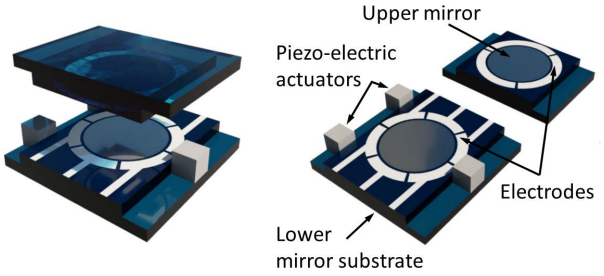

FIGURE 1. Exploded schematic view of a Fabry-Perot interferometer used in this work. The aperture diameter is 15 mm. Electrical connections are made to the electrodes on the lower mirror substrate and to the piezoelectric actuators.

so that only one narrow wavelength band is transmitted at a time.

Fig. 1 shows the principle of the FPI used in this work. This FPI module has an optical aperture of 15 mm in diameter and a mass of 30 g. It is designed for operation at low orders of interference ($N = 4 \ldots 14$) in the wavelength range from 250 to 370 nm. The gap is measured by measuring the capacitance between three sets of electrodes and adjusted by three piezoelectric actuators. The role of the FPI controller is to adjust the drive voltages of the actuators that set the gap and thus the transmitted wavelength. In addition to adjusting the gap, the controller must maintain the mirrors parallel. A tilted mirror gap would cause the transmission wavelength to vary over the aperture. This instrument is often referred to as a capacitance-stabilized etalon (CSE).

Two parameters were fundamental during the development of the FPI controller for ALTIUS: noise and temperature-induced drift. Noise generated by the controller causes a fluctuation of the mirror gap and an apparent spectral broadening of the transmission bands. Temperature variations affect the control electronics by shifting the transmission wavelength away from the target value. With cascaded FPIs, the optical throughput suffers if the transmission bands drift apart. The combined effect of noise and temperature drift on the gap should be limited to less than 0.1 nm for an electrode distance of 3 μm over the operating temperature range –45 to +60 °C. This drift corresponds to a temperature coefficient of 0.3 ppm/°C, a formidable requirement considering the type of components available.

Earlier reported FPI controllers are based on the design of Hicks *et al.* [4]. In these controllers, two channels adjust mirror parallelism using two pairs of electrodes on the FPI, while a fifth capacitor and one controller channel determine the mirror gap. The controller designed in this work allows a more straightforward electrode arrangement on the FPI, using only three gap-dependent capacitances.

The novelty of the controller implemented in this study is the method for the voltage excitation of the capacitive bridges used to estimate the gap. The capacitance bridges are excited by square wave, pulse-amplitude modulated signals. The signals feeding the pulse-amplitude modulators (PAM) are generated by fractional-N-based pulse-width modulators (PWM). Three signals with programmable amplitude are generated for the gap set points, and one signal with constant amplitude is used as a reference.

All four signals are produced by identical PWM and PAM stages. With this arrangement, the ratio of the excitation signals of each capacitance bridge is stable, even if the supply voltage for the PWM switches varies. As shown in Section 3, the gap stability depends on the ratio of the excitation voltages and not on their absolute values.

The Fabry-Perot interferometer used in this study is described in Section 2, and the operating principle of the FPI controller electronics is described in Section 3. Section 4 deals with the control loop. The magnitude of the errors induced by electronic noise and the effect of temperature drift are addressed in Section 5 through simulations and measurements. Finally, the noise contributions of individual circuit blocks are presented. In this section, the term noise accounts for unwanted fluctuations of the FPI mirror gap. For this discussion, a lower frequency limit of 1 Hz was chosen, whereas the upper limit of 20 kHz was determined by the dynamic properties of the FPI. The frequency range below 1 Hz was studied as temperature-induced variations of the gap.

To the best of our knowledge, the stability of the FPI controller presented in this work exceeds that of previously reported controllers. The gap noise and the temperature-induced drift of the controllers reported in previous studies are compared to that of the ALTIUS controller in Section 6.

II. THE FABRY-PEROT INTERFEROMETER

The Fabry-Perot interferometer, for which this controller was designed, is a tunable, parallel-mirror, low-order, lightweight module intended for use as a wavelength-selection filter in a hyperspectral imager. Similar FPIs were used in, for example, the hyperspectral cameras of the nanosatellites Aalto-1 [6] and PICASSO [7]. The FPI consists of three main components as shown in the exploded schematic view of Fig. 1. Both the upper and lower substrates have semi-transparent mirrors, deposited electrodes, and piezoelectric actuators. The substrates are typically made of fused silica or synthetic sapphire, depending on the operating wavelength. Depending on the specifications, the mirror surfaces are metallic or a stack of dielectric thin films.

Piezoelectric actuators are robust components for position control in the micrometer to the sub-nanometer range. This type of actuator exhibits hysteresis and creep, which makes it difficult to adjust the mirror gap without position feedback control. Piezoelectric actuators can be used without position feedback if the charge delivered to or drained from the actuator is controlled. Ouattara *et al.* designed a driver for piezo-actuated FPIs that achieved a reduction of the hysteresis, without position feedback, by up to 98% [8].

Li *et al.* [9] and Li and Shan [10] proposed a numeric decoupling inverse hysteresis compensator to mitigate coupled hysteresis effects. When used in a closed-loop system, they pointed out that hysteresis effects cause inaccuracy,

oscillation, and instability. However, the results of this study do not support this statement.

The movement of the actuators, and thus the distance between the mirror substrates, is monitored by changes in the capacitance between the electrodes deposited on the substrates, as shown in Fig. 1. The metallic electrodes are deposited in three 120° sectors around the mirrors. On the lower substrate, each electrode is split in the middle to form – together with the slightly smaller electrode on the upper substrate – a series connection of two variable capacitances. This arrangement keeps the upper substrate free of electrical connections; all connections are made to bonding pads on the lower substrate. Each capacitor pair is used in a servo loop controlling the adjacent piezoelectric actuator. The electrodes are connected to preamplifiers on a circuit board surrounding the FPI.

The arrangement of the electrodes of the gap-sensing capacitors is shown in Fig. 2. For each of the three gap control channels, the capacitors comprise three electrodes, two on the lower substrate and one slightly larger on the upper substrate. Only the electrodes on the lower substrate are connected to the capacitance bridge.

While the capacitance between two plane electrodes is primarily determined by the area and the distance between them, the tilt angle also affects the capacitance. The use of three capacitive sensors around the optical aperture and always aiming for a parallel gap makes electrode tilting in this application a non-issue. The division of the measurement capacitances into two parts leaves the electrode on the upper mirror substrate floating. Stray capacitances between the electrodes and surfaces surrounding the FPI affect the gap measurement. With the FPI installed in a conductive housing, the changes in the stray capacitance are small, and this effect is negligible. With a substrate thickness of 6.35 mm and a distance between the upper substrate and the housing of 1 mm, a change in this distance affects the mirror gap by a factor of approximately $0.3{\cdot}10^{-6}$.

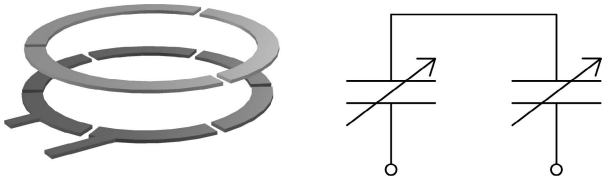

FIGURE 2. Arrangement of the electrodes of the gap-sensing capacitors on the upper and lower substates of the FPI. Only two of the six bonding areas are drawn. On the right is a schematic representation of the resulting series connection of one pair of capacitors. In the following schematics, the series connection is drawn as one variable capacitor, Cfpi.

III. THE FPI GAP CONTROLLER

In this work, circuit simplicity was essential, and a basic closed-loop concept was chosen based on position feedback and voltage amplifiers for the piezo actuators. The FPI electronics are based on three main parts:

- Piezo-electric actuators, adjusting the distance between the FPI mirror substrates and measurement electrodes,
- The electrodes on the FPI, forming a variable, gap-dependent capacitance, and
- A feedback controller, maintaining the set values for the FPI capacitances, and thus the gap.

The FPI controller developed and described in this study uses component types that are available with the quality level and radiation tolerance required for a satellite instrument. The controller prototypes use commercial-grade components that are representative of the corresponding space-grade parts. No precision components are used.

The block diagram in Fig. 3 shows the main elements of one of the three identical gap control loops. The components in the middle of the figure, within the dashed line, are situated inside the FPI housing. The other parts are located in the controller unit at a distance of 1 to 2 m from the FPI.

The FPI capacitance is not measured directly; instead, it forms part of a capacitive half-bridge, balanced by the servo loop. The imbalance signal is used in a feedback loop that controls the voltages to the piezo-electric actuators, thereby determining the gap between the mirror substrates. The actuators are mounted between the mirror substrates and directly determine the distance between the electrode pairs making up the capacitor Cfpi in Fig. 3. The upper arm of the half-bridge is a fixed ceramic class 1 capacitor, Cref, which acts as the reference capacitance. The amplified and band-pass filtered imbalance signal is rectified using a phase-sensitive detector (PSD). The output is a baseband, low-frequency signal proportional to the difference between the commanded and actual gaps. Finally, a PI-controller feeds the piezo amplifier and the piezo actuator adjusting the gap to null the error signal.

With V_{ref} and V_{sp} designating the excitation voltages of the capacitance bridge, and C_{ref} and C_{fpi} the fixed reference capacitance and the FPI electrode capacitance, the imbalance or error voltage V_{err} at the input to the preamplifier can be written using Laplace transform designators as

$$V_{\mathrm{err}}(s) = \frac{V_{\mathrm{sp}}(s)sC_{\mathrm{fpi}} + V_{\mathrm{ref}}(s)sC_{\mathrm{ref}}}{sC_{\mathrm{fpi}} + sC_{\mathrm{ref}} + sC_{\mathrm{par}}}, \tag{1}$$

where C_{par} is the sum of the parasitic capacitances at the preamplifier input and s is the complex frequency. The voltage at the lower end of the bridge, V_{sp}, is here called the setpoint voltage, as this is used to control the gap. There is a capacitive coupling between the connections to the FPI electrodes on the preamplifier circuit board. This capacitance directly adds to the FPI electrode capacitance.

If the gap controller and the piezo actuator, manipulating the capacitance C_{fpi}, can balance the bridge, that is, set V_{err} to zero, (1) reduces to

$$V_{\mathrm{sp}}(s)sC_{\mathrm{fpi}} + V_{\mathrm{ref}}(s)sC_{\mathrm{ref}} = 0,$$

when

$$sC_{\mathrm{fpi}} + sC_{\mathrm{ref}} + sC_{\mathrm{par}} \neq 0. \tag{2}$$

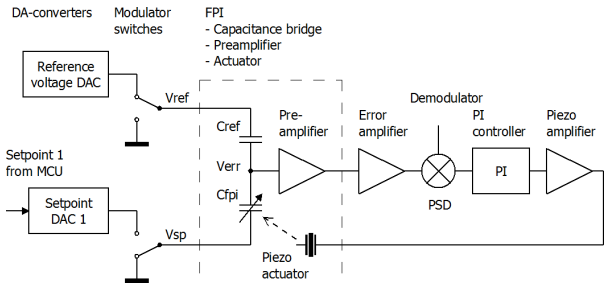

FIGURE 3. Block diagram of the FPI gap control loop. The FPI gap controller is built using three identical control loops. The dashed line indicates the housing of the FPI unit. Blocks outside the FPI are part of the controller. A setpoint command is a digital number being converted to the corresponding DC voltage in the DA-converter block.

A requirement for nulling is that the waveforms V_{sp} and V_{ref} fulfill the requirement

$$V_{\mathrm{sp}}(s) = -kV_{\mathrm{ref}}(s), \quad k \geq 0. \tag{3}$$

The setpoint waveform must be a scaled copy of the reference waveform V_{ref} at the opposite phase, and the factor k is directly proportional to the setpoint value. In this work, square wave signals are used for V_{ref} and V_{sp}.

The aluminum electrodes are deposited on an area etched down approximately 0.7 μm from the active mirror surface. With d_{e} designating the etching depth of each substrate and d the mirror distance, the electrode capacitance can be approximated as

$$C_{\mathrm{fpi}} = \frac{\varepsilon_{\mathrm{r}}\varepsilon_0 A}{2(d + 2d_{\mathrm{e}})}, \tag{4}$$

where ε_{r} is the relative permittivity of the gas between the electrodes, ε_0 is the permittivity of vacuum, and A is the area of an electrode on the lower substrate. The factor two in the denominator is due to the two series-connected capacitor halves. Equation (4) ignores edge effects and assumes a parallel gap. For the FPI used in this study, the values in (4) are $A = 15{\cdot}10^{-6}$ m^2, and $d = 400$ to 1400 nm, giving a capacitance value of 37 to 24 pF. At an etching depth of $d_{\mathrm{e}} = 700$ nm, the capacitance change is 19 fF/nm at the small gap and 9 fF/nm at the upper end. If the FPI is not operated in a vacuum, the permittivity is affected by, e.g., humidity, temperature, and pressure. Humid air should be avoided, as water can be adsorbed on the electrodes [11].

Inserting the expression for C_{fpi} into (2) gives, at nulled error,

$$d = \frac{k\varepsilon_{\mathrm{r}}\varepsilon_0 A}{2C_{\mathrm{ref}}} - 2d_{\mathrm{e}}. \tag{5}$$

The gap is directly proportional to the commanded setpoint, k, which is the ratio of V_{sp} to V_{ref}; the actual values of the excitation voltages are unimportant. This characteristic eases the requirements on the circuitry that generates the excitation signals for the capacitance bridge.

In this application, absolute electrode capacitance values are not required. However, owing to differences in the reference and stray capacitances, the parallelism and gap of the FPI must be determined by calibration.

With a reference voltage of 2 V, the ratio of error voltage to gap change is of the order of 0.3 to 0.6 mV/nm; the larger the gap, the lower the sensitivity.

The error signal Verr in Fig. 3 is buffered by a preamplifier located close to the FPI and further amplified by the error amplifiers in the control unit. Only a buffer amplifier is located in the FPI housing to maintain low power dissipation near the FPI. The buffered error signal is fed via a cable to the gap controller at a thermally less critical location.

A. BRIDGE EXCITATION

The reference and setpoint square wave voltages are generated by analog CMOS multiplexers of type 4053. This switch is listed in the European Space Component Coordination's Qualified Parts List [12] as 4053B in the 4000B series and 54HC4053 in the high-speed CMOS logic series. Automotive-grade 74HC4053 switches were used in the prototype. The switch for the reference signal, feeding Cref in the upper arm in Fig. 3, connects the bridge to ground potential or a DC reference voltage, alternating with a nominal duty cycle of 50% and a frequency of 29 kHz. Similarly, the lower arm is connected to a DC setpoint voltage or ground. The signals controlling the switches are phase-shifted by 180°.

In, for example, the spectral camera of the nanosatellite Aalto-1, the setpoint voltages were generated using D/A-converter ICs feeding the pulse amplitude modulator (PAM) switches. For this work, suitable space-grade D/A-converters were unavailable, and they were replaced by digitally controlled pulse-width modulators and low-pass filters. A D/A-converter based on pulse-width modulation can be implemented using a counter, a magnitude comparator, a switching element, and an RC low-pass filter.

In a basic pulse-width modulator, the output of a continuously running binary counter is compared to the digital setpoint command value. The output is high if the counter output value is less than the setpoint. For the remaining time of the counter period, the output is low. With a counter period of N clock cycles, and a setpoint value of k, the duty cycle of the PWM signal is k/N. The duty cycle can get N different values. The frequency of the PWM signal is f_{clk}/N, where f_{clk} is the frequency of the counter clock. In this application, the setpoint resolution requirement is 16 bits, i.e., $N = 65536$. With the frequency of the capacitive bridge excitation set to 29 kHz, the PWM output is chosen as twice this frequency, 58 kHz, to obtain a complete cycle of the PWM signal for half a cycle of the bridge excitation. A counter clock frequency of $65536 \cdot 58$ kHz ≈ 3.8 GHz would be necessary. This frequency is beyond the clock frequency range of the FPGA used for the PWM counters.

Two modifications of the basic PWM-based digital-to-analog converter (DAC) were tested: a combination of a coarse and a fine stage and the use of dithering of the PWM signal. In contrast to the case of DACs based on, for example, integrated circuits using resistor networks, it is possible to combine the outputs of two PWM-based DACs to achieve the required resolution and linearity without the exceedingly high

frequency of the PWM counter clock. However, this concept requires two PWM switches with their corresponding drive signals for each DAC combination; one coarse and one fine. In this application, the number of signal lines between the FPGA containing the PWM counters and the analog section with the PWM switches became too high.

Instead, an 11-bit binary counter was used, providing a pulse frequency of 58594 Hz from the 120 MHz system clock. Taking a group of 32 pulses and extending 0 to 31 of them by one clock cycle (8.33 ns) gives, on average, a mean duty cycle corresponding to the 16-bit input code. Consider a repeating group of M PWM pulses, each with a period of m clock cycles, giving the total length of the pattern of Mm clock cycles. Of these PWM pulses, K pulses have a width of n clock cycles, while the remaining $M-K$ pulses are one clock cycle longer, $n+1$ clock cycles. The average duty cycle is then

$$\langle \eta \rangle = (Kn + (M - K)(n + 1))\big/(Mm), \tag{6}$$

where the angle brackets denote averaging over groups of M pulses. The values of n and K are determined from the input code N as $n = \text{int}(N/M)$, and $K = N \bmod M$, that is, the remainder of the division of N by M. By choosing the pulse group length as a power of two, the input code can be split into the upper bits giving the base pulse width n, and the lower bits determining the number of pulses to stretch. For example, with a 16-bit input code and an 11-bit PWM counter, the base pulse period is $m = 2^{11} = 2048$ clock cycles, and the total pattern length is $M = 2^5 = 32$ pulses, or 65536 clock cycles.

The extended pulses are distributed evenly within the group to keep the amplitude of the subharmonics, that is, integer fractions of the pulse frequency, as low as possible. The position of the extended pulses can be determined by a fixed look-up table addressed by the number of pulses to stretch. The pulse extension is shown, exaggerated, at the down arrows on the Setpoint PWM waveform in Fig. 5.

Fig. 4 shows the principle of the circuitry for generating the bridge excitation signals. Inverters of type 54AC04 are used as the PWM switches. In Fig. 4, this inverter is drawn only as the on-resistances of the output transistors and an ideal switch. The input signal of the inverter controls the switch. The PWM switch is loaded by the low-pass filter Rlp Clp. If the time constant of this RC-filter is high, the voltage across the capacitor, V_{dc}, can be considered constant:

$$V_{\text{dc}} = \frac{V_{\text{dd}}\eta\left(R_{\text{l}} + R_{\text{lp}}\right)}{\eta\left(R_{\text{l}} - R_{\text{h}}\right) + \left(R_{\text{h}} + R_{\text{lp}}\right)}, \tag{7}$$

where V_{dd} is the voltage at the switch high-side, i.e., the supply voltage of the inverter, and η is the switch duty cycle. R_{h} and R_{l} designate the on-resistances of the high- and low-side switch elements, in this case, the drain-source on-resistances of the P- and N-channel output MOSFETs of the 74AC04 inverter output stage. The off-resistances are assumed to be infinite. The term (R_{l}–R_{h}) in the denominator introduces a nonlinearity into the transfer function. The greater the difference R_{l}–R_{h}, the greater the nonlinearity. Using digital-to-analog converter terminology, the deviation from a linear response is the integral nonlinearity, INL. However, in the FPI controller case, the INL is irrelevant, as calibrating the entire FPI system takes care of the effect.

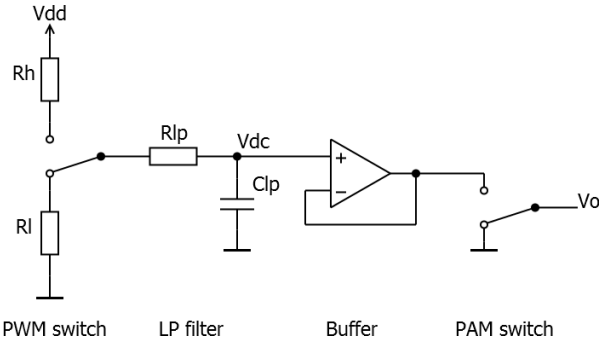

FIGURE 4. Generation of the bridge excitation voltages. Rh and Rl represent the on-resistances of the inverter acting as the PWM switch. Rlp and Clp make up a low-pass filter feeding a DC-signal, Vdc, to the buffer amplifier. The output of the PAM switch, Vo, is fed via a cable to the capacitance bridge in the FPI unit. Each FPI controller uses four identical circuits, generating, as Vo, the reference waveform Vref, and the three setpoint waveforms, Vsp. Individual counters control all the switches.

The temperature dependency of the switch on-resistances is more critical. The temperature effect can be mitigated by a high ratio of load resistance, R_{lp}, to switch resistances. For example, the 74AC04 inverter used in the prototype has an on-resistance of $R_{\text{l}} = 10\ \Omega$ and $R_{\text{h}} = 19\ \Omega$ and a temperature coefficient of on-resistance of 0.001 1/°C.

According to (7), a large value of R_{lp} mitigates the effect of varying switch resistances. An upper limit is set by the bias current drift of the buffer amplifier. In the prototype, R_{lp} was 250 kΩ, with $C_{\text{lp}} = 22$ nF, dictated by the settling time of the low-pass filter.

The supply voltage of the PWM switches is 3.3 V, regulated by a linear regulator. The stability requirement for the supply voltage is not critical as long as all PWM switches are supplied from the same rail; only the ratios of the voltages feeding the capacitance bridges are essential.

The low-pass filtered PWM signals are applied to the modulator switches, generating square wave signals feeding the capacitance bridge. Even if the amplitude of the reference signal is constant at approximately 2 V, it is still generated by a pulse-width modulator and low-pass filter identical to those that generate the setpoint signals. The reference signal level can be adjusted such that the setpoint voltage range corresponds to the mirror gap range used.

For convenience, the bridge excitation frequency is chosen as $f_{\text{clk}}/2N$, where f_{clk} is the clock frequency of the FPGA block generating all switching signals. The capacitance of the measurement bridge, $C_{\text{ref}} + C_{\text{fpi}} + C_{\text{par}}$, feeding the preamplifier with the biasing resistance R_{bias}, creates a high-pass filter with a cut-off frequency $f_{\text{HP}} = 1/(2\pi C_{\text{tot}} R_{\text{bias}})$, or ca 1 kHz. The bridge excitation frequency should be higher to avoid excessive attenuation of the error signal. With square wave excitation, the switching moments, especially switching time errors, give rise to gap errors, compensating for the effect of imperfect switching. The more often switching occurs, the larger is the error. The frequency of the PWM modulation of

reference and setpoint signals is 58 kHz. With the reference signal and the setpoint signal both containing an entire period of the PWM cycle, the bridge excitation frequency is set to 29 kHz.

Fig. 5 shows a schematic timing diagram of the signals in the FPI controller during an increase in the commanded setpoint. The uppermost three waveforms refer to the reference signal, the middle three to the setpoint, and the lowest three to the error signal, the demodulated error, and the output of the PI-controller or piezo amplifier. At the arrow, the commanded setpoint is changed: the PWM duty cycle, the filtered DC level, and the amplitude of Vsp increase. Simultaneously, the error signal amplitude increases due to the imbalance of the capacitance bridge. The demodulated error at the PSD output drives the PI-controller to increase the voltage to the piezo actuator (lowest waveform). Consequently, the gap increases, the capacitance C_{fpi} decreases, and the system returns to a new steady state with a nulled bridge.

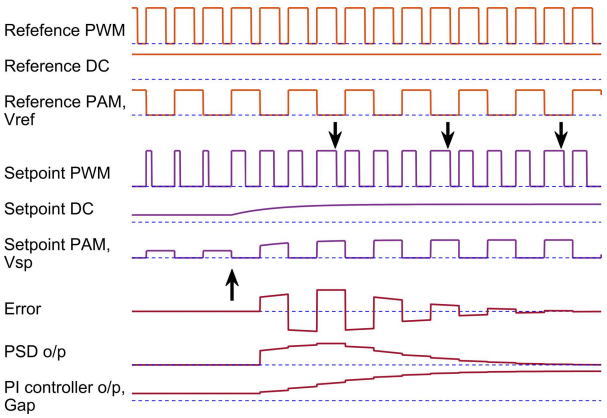

FIGURE 5. Schematic timing diagram of the signals in the FPI controller. The down arrows indicate PWM pulses that are extended with one base clock cycle to meet the required average pulse width. The waveforms are not to scale.

B. PREAMPLIFIER

Fig. 6 shows a simplified schematic of the preamplifier. The first transistor is an N-channel JFET, 2N4858, followed by a common-emitter coupled PNP BJT, 2N3904. The voltage gain from the mid-point of the capacitance bridge to the load resistor Rload is 0.95. The amplifier serves only to buffer the error signal and drive the cable to the FPI controller. The idle voltage across the 1 kΩ load resistor, Rload, is 2 . . . 3 V, determined by the pinch-off voltage $V_{\text{GS,off}}$ of the JFET. The capacitance value of Cref is 47 pF.

The accumulated radiation dose of the JFET causes an increase in the gate leakage current. The gate bias resistor has a value of only 3.3 MΩ, allowing a considerable increase in the gate leakage current while maintaining the amplifier operational.

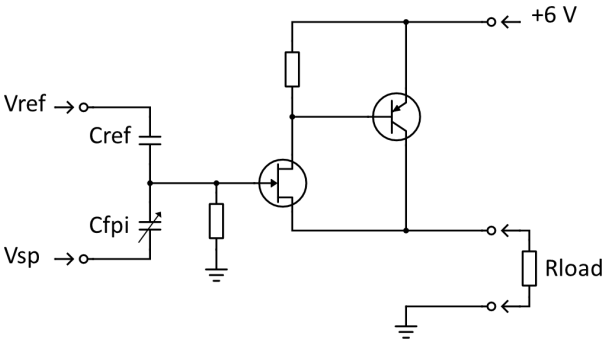

FIGURE 6. Schematic diagram of the preamplifier located in the FPI unit. Vref and Vsp are supplied from the FPI controller. The load resistance Rload is located in the controller. Components for ESD protection are omitted for clarity.

C. SQUARE WAVE EXCITATION AND THE INHIBIT SWITCH

In practice, the requirement of (3), $V_{\text{sp}} = -k\ V_{\text{ref}}$, is difficult to satisfy using square wave excitation. The requirement states that the shapes of the waveforms are the same, differing only by a negative scaling factor. The high-to-low switching of the reference signal must coincide with the low-to-high transition of the setpoint signal and vice versa. If this is not the case, the error signal will have switching residuals with an amplitude approaching half the amplitude of the excitation signals. These transients are not related to bridge imbalance. However, the demodulated error signal may still require a compensating shift in the capacitance ratios to re-null the error signal. The PI-controller introduces a real bridge imbalance to compensate for the false error signal. Unfortunately, the transients can also overdrive the input stage of the error amplifier.

Equation (3) holds for the excitation voltages, V_{ref} and V_{sp}, right at the capacitance bridge. The generation of the reference and setpoint excitation waveforms introduces series impedances and timing issues that make it difficult to satisfy the requirement of (3). Sources of imperfections include the following:

- Different high-side and low-side on-resistances of the PAM switches that generate the square wave excitation voltages V_{sp} and V_{ref},
- Differences in on-resistances between the reference and setpoint switches,
- Difference in propagation delays of the switches,
- Differences in the timing of the control signals of the switches, and
- Differences in cable impedances for the reference and setpoint signals to the bridge.

All of these cause transients in the error signal. This transient is filtered in the error amplifier and demodulated as the actual imbalance signal. The transient might require a compensating capacitance imbalance to compensate for its effect at the input of the PI-controller. The compensating signal is generated by shifting the gap from its ideal position, thereby introducing a deviation from the desired gap.

In the prototype FPI controller, the effect of excitation signal asymmetry was mitigated using a switch that disconnects the error amplifier just in time before the transients and reconnects it when the switching transient has decayed. The switch is shown in Fig. 7.

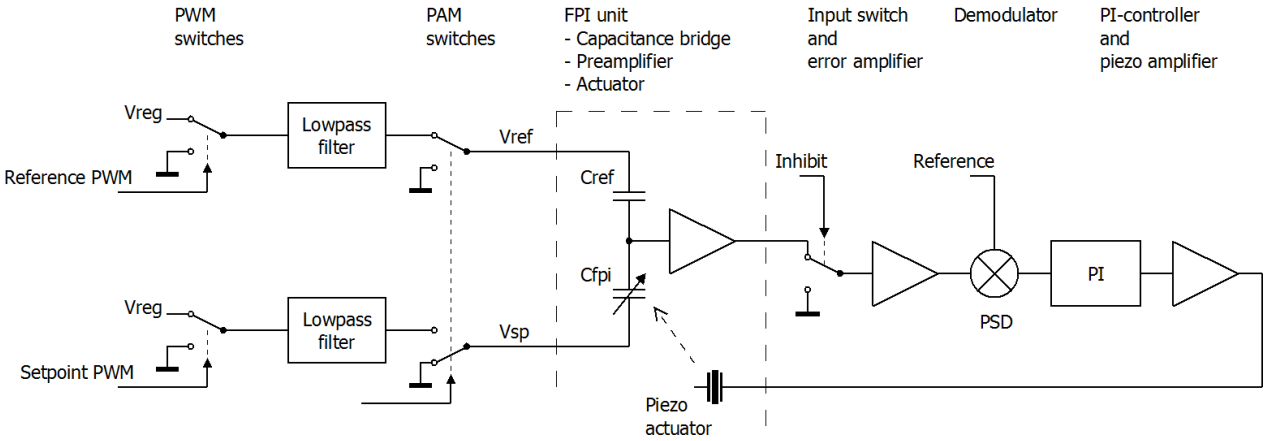

FIGURE 7. One of the three gap control channels with the inhibit switch. The switch disconnects the signal to the error amplifier during switching transients.

Charge injection from the 4053-type inhibit switch generates a new type of disturbance at the input of the error amplifier. The switch operates at twice the error signal frequency, as there are two level changes of the bridge excitation per period. Thus, the switch-induced disturbance has a dominant frequency that is twice that of the proper error signal. In the controller prototype, the inhibit switch operated at 58 kHz, twice the signal frequency of 29 kHz. The phase-sensitive demodulator attenuates the 58 kHz signal while demodulating the 29 kHz error signal.

The effectiveness of the input switch was measured by shifting the switching instants of the setpoint PAM modulators with respect to those of the reference signal, thus mimicking the factors that could induce asymmetry in the bridge excitation. The rising and falling edges of the setpoint signal were shifted in steps of 8 ns. The use of the inhibit switch decreased the effect on the gap by a factor of five. At an electrode gap of 2 μm, the gap change decreased from 10 pm/ns to 2 pm/ns, or, as a relative change, from 5 ppm/ns to 1 ppm/ns.

A corresponding decrease in temperature sensitivity was observed by varying the controller temperature between –50 and 50 °C. Temperature-induced drift was measured by monitoring the change of the gap of an FPI held at a constant temperature. With the inhibit switch enabled, the change in electrode gap decreased from 120 ppm to 30 ppm over a temperature change of 100 °C. These gap changes are expressed using the box method: a rectangle is drawn enclosing all the measurement points, and the given values are the height and width of the rectangle. The measurement uncertainty is approximately 20 ppm.

The benefit of the inhibit switch must be judged on a case-by-case basis. The switch improves controller performance but increases the number of components.

D. ERROR AMPLIFIER AND DEMODULATOR

After the optional inhibit switch, the imbalance signal is fed to the error amplifier. This amplifier, implemented using operational amplifiers in two stages, has a band-pass response

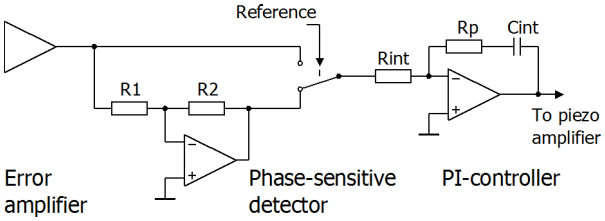

FIGURE 8. Error amplifier, PSD, and PI-controller. The lower path of the PSD has a gain of –1 (R1 = R2). The switch, a 4053-type analog multiplexer, is controlled at the same frequency as the bridge excitation, 29 kHz.

with a maximum gain of 35 dB at the carrier frequency of 29 kHz. A phase-sensitive detector, PSD, demodulates the amplified error signal.

The PSD in the prototype controller consists of a switch (4053), which connects either the output of the error amplifier or the inverted error signal, that is, multiplied by –1. It can be considered a multiplier that multiplies the amplified error signal by a square wave with values –1 or 1. A schematic of the block is shown in Fig. 8. The PSD operates at the same frequency as the bridge excitation. The phase of the signal controlling the switch is set to match the phase of the fundamental frequency of the amplified error signal. Ideally, the PSD phase coincides with the excitation of the capacitance bridge, but the inhibit switch and phase shifts in the error amplifier may require different timing. Typically, the PSD is followed by a low-pass filter. In this case, the integrator and piezo amplifier perform this function. The PSD functions as a mixer, shifting the error signal at the carrier frequency of 29 kHz down to the baseband, 0 to 1 kHz.

As Blair and Sydenham point out in [13], the term phase-sensitive detector can be confusing in this mode of operation. This is because the phase difference between the amplified error signal and the reference signal is constant, and the PSD acts only as a signed amplitude detector.

The PSD also mixes the noise of the error signal to the baseband. In addition to the noise at the carrier frequency f_c, a square wave-fed mixer adds noise shifted down from odd harmonics, 3 f_c, 5 f_c, and so forth. Without band-pass or low-pass filtering of the error signal, the square-wave-fed

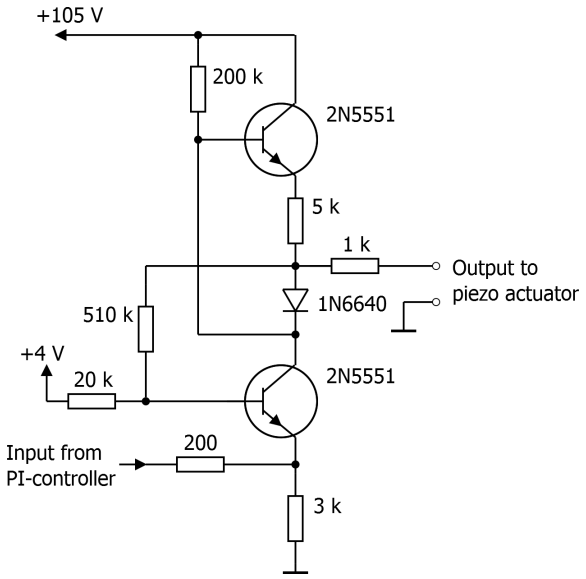

FIGURE 9. Schematic diagram of one of the piezo amplifiers. Resistance values are in ohms.

PSD outputs a noise level several decibels higher than that of a sine-wave-fed mixer. This noise penalty can be mitigated by band-pass filtering of the error signal before the PSD, thus attenuating the noise images produced by the harmonics.

The output of the demodulator, a measure of bridge imbalance now at baseband frequencies, is input to the PI-controller, which drives one of the three piezo amplifiers.

E. PI-CONTROLLER AND PIEZO AMPLIFIER

The demodulated error signal is fed to the PI-controller based on an operational amplifier (see Fig. 8). The piezo amplifier, shown in Fig. 9, raises the voltage at the output of the PI-controller to a level suitable for the piezo actuators, in this case, from 0 to 100 V. The amplifier is based on two transistors of the same bipolar NPN type, 2N5551. The base current of the upper transistor is fed via a 200 kΩ resistor, which decreases the available base current at high output voltages. This decrease in the base current lowers the positive slew rate for high output voltages. In this application, this source of signal distortion affects only large gap steps. The piezo amplifier typically operates in a quasistatic state, maintaining the FPI at a constant gap.

The design of the piezo amplifier was driven by low idle power consumption, tolerance to a reduction in the current gain of the transistors due to radiation, and a low number of components. According to simulations, the amplifier performs adequately even after reducing the transistor current gain from a value above 150 to below 50. The piezo actuator represents a large load capacitance of 380 nF. A resistor of 1 kΩ in series with the piezo actuator ensures stability. A higher value improves the stability margins of the amplifier but worsens the gain margin of the entire servo loop.

In the prototype, a commercial DC/DC-converter produced the supply voltage of 105 V for the piezo amplifier. The idle current consumption was 0.5 mA per amplifier.

IV. CONTROL LOOP

The FPI controller prototype was built as three independent servo loops, each driving one of the three piezoelectric actuators of the FPI. The gap control loop is broken down into blocks, as shown in Fig. 10.

The FPI mirror gap is estimated by nulling three capacitive half-bridges, each composed of the varying capacitance between the electrodes on the FPI and a fixed reference capacitor. An FPI unit contains three identical capacitance bridges and their preamplifiers. The bridge is excited by the reference and setpoint signals generated by the FPI controller. The bridge imbalance, or error signal, is fed to the preamplifier, which lowers the impedance level to a level compatible with driving the cable to the FPI controller, as well as the load impedance of the FPI controller. The error amplifier in the FPI controller amplifies this 29 kHz error signal. A phase-sensitive detector demodulates the error signal to a baseband signal fed to a PI-controller, which further feeds the piezo amplifier. The voltages fed to the three piezo actuators in the FPI unit determine the gap between the FPI mirror substrates and, therefore, the capacitance between the electrodes, closing the control loop.

The FPI causes cross-coupling between the channels; the movement of one piezo actuator affects the gap of all three channels. Cross-coupling is excluded from the one-channel model.

The input to the block named ‘‘FPI electrodes’’ is the main entry point for external disturbances. In addition to coupling from the other channels, thermal effects also affect the gap.

The designation of transfer functions used for each block is presented in Table 1.

A. SETPOINT FILTER

The setpoint filter corresponds to the PWM low-pass filter and is not a part of the control loop. It affects, however, e.g., the step response.

B. ERROR AMPLIFIER AND DEMODULATOR

The error amplifier has a band-pass characteristic with a center frequency of 29 kHz and a bandwidth (–3 dB) of ca 20 kHz. The gain from the gap imbalance signal to the output of the demodulator is $G_{\mathrm{ErrAmp}} = 37$ dB, including the preamplifier gain, –0.5 dB, and the demodulator gain, –1 dB. The blocks operating at 29 kHz are considered constant gain blocks in the baseband loop analysis.

C. PI-CONTROLLER/COMPENSATOR

In the prototype, the proportional gain of the PI-controller was set to zero, resulting in a transfer function $G_{\mathrm{Comp}}(s) = 142/s$. A non-zero P-gain improves the step response, but the effect of the mechanical resonances of the FPI is emphasized. This transfer function is valid from approximately 1 mHz to 100 kHz. The lower limit is set by the gain of the operational amplifier and the upper limit by its output impedance.

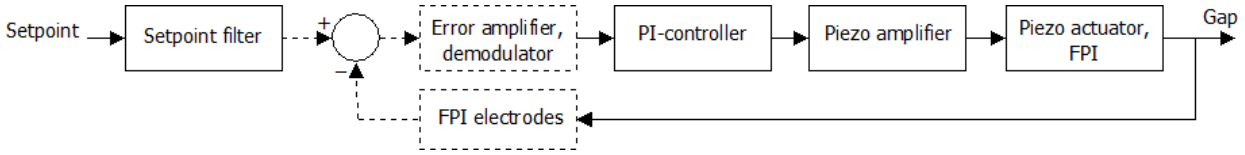

FIGURE 10. Block diagram of one of the gap control loops. Blocks and signals drawn with dashed lines operate at the carrier frequency, 29 kHz.

TABLE 1. Designations for transfer functions of the control loop.

Block	Design.	Input	Output
Setpoint filter	$G_{SP}(s)$	Digital number	Setpoint voltage
Error amplifier, demodulator	G_{ErrAmp}	Setpoint voltage, electrode capacitance	Demodulated error signal
PI-controller	$G_{Comp}(s)$	Demodulated error signal	Control voltage
Piezo amplifier	$G_{PA}(s)$	Control voltage	Piezo drive voltage
Piezo actuator, FPI	$G_{FPI}(s)$	Piezo drive voltage	Gap at electrodes
FPI electrodes	dC_{fpi}/dd_e	Gap at electrodes	Electrode capacitance

Note: The setpoint filter is not part of the loop.

D. PIEZO AMPLIFIER

The NPN transistors (2N5515) used in the piezo amplifier are the components of the FPI controller which are the most sensitive to ionizing radiation. The radiation dose affects the current gain of the transistors. A change in the current gain affects the amplifier bandwidth, and the initial and degraded current gains must be considered in the loop stability assessment. A decrease in the current gain from a maximum specified $h_{FE} = 250$ to the worst-case post-radiation value $h_{FE} = 40$ decreases the frequency of the first pole of the amplifier small-signal transfer function from 300 Hz to 200 Hz. The low-frequency gain decreases from 27 to 26 dB.

E. PIEZO ACTUATOR AND FPI

The transfer function of the FPI from the piezo voltage to the gap was estimated by feeding a test signal with varying frequency to one piezo actuator at a time while measuring the capacitance change of each of the gap electrodes. The resulting 3×3 transfer function matrix, describing multiple resonances and anti-resonances between 10 and 25 kHz, was simplified for this analysis to the second-order system $G_{FPI}(s)$ with a single resonance at 11 kHz:

$$G_{FPI}(s) = \frac{0.020}{2.3 \cdot 10^{-10} s^2 + 4.5 \cdot 10^{-7} s + 1}. \tag{8}$$

The unit of $G_{FPI}(s)$ is μm/V.

F. FPI ELECTRODES ANFD CAPACITANCE BRIDGE

With (4) giving the electrode capacitance as a function of the gap, the capacitance variation with the electrode distance can be written as

$$\frac{dC_{fpi}}{dd_{ele}} = -\frac{\varepsilon_r \varepsilon_0 A}{2d_{ele}^2}, \tag{9}$$

where $d_{ele} = (d + 2d_e)$ is the total electrode distance. The rate of change varies between –37 pF/μm and –14 pF/μm for electrode gaps $d_{ele} = 1.7$ μm and 2.8 μm.

Taking the derivative of (1) with respect to C_{fpi} gives the sensitivity of the bridge error signal to changes in the electrode capacitance,

$$\frac{dV_{err}}{dC_{fpi}} = \frac{V_{sp}}{C_{fpi} + C_{ref} + C_{par}} - \frac{V_{sp} C_{fpi} + V_{ref} C_{ref}}{\left(C_{fpi} + C_{ref} + C_{par}\right)^2}. \tag{10}$$

With V_{sp} and V_{ref} representing signals of opposite phase, the numerator of the second term on the right-hand side equals zero at bridge equilibrium. For small capacitance changes, the expression simplifies to

$$\frac{dV_{err}}{dC_{fpi}} = \frac{V_{ref} C_{ref}}{C_{fpi}} \frac{1}{C_{fpi} + C_{ref} + C_{par}}. \tag{11}$$

The bridge sensitivity to gap change is

$$\frac{dV_{err}}{dd_{ele}} = \frac{dV_{err}}{dC_{fpi}} \frac{dC_{fpi}}{dd_{ele}}, \tag{12}$$

which amounts to 700 mV/μm for small gaps and 570 mV/μm for large gaps. The resulting change in loop gain is approximately 2 dB.

G. LOOP GAIN

Fig. 11 shows the simulated loop gain obtained by multiplying the individual transfer functions in Table 1. The gain and phase margins are summarized in Table 2 for the worst cases: low gain of the piezo amplifier transistors combined with a large gap, and on the other hand, high gain and a small gap. Fig. 11 also shows the measured loop gain. This measurement was performed using an additional summing junction amplifier stage between the PI-controller and the piezo amplifier. Using this amplifier, the excitation signal from a signal analyzer (HP 89410A) could be fed into the control loop without disturbing the circuit's source and load impedance relations. The analyzer measured the output of the PI-controller as well as the output of the summing amplifier, and the loop gain was estimated from these measurements. The difference between the measured (dotted) and the simulated gains is due to the need for high excitation at high frequencies. The high excitation signal level caused distortion in the piezo amplifier, manifesting as a seemingly lower gain above 200 Hz.

Reference [14] defines the phase margin as the difference between the phase of the open-loop transfer function and –180° (modulo 360°) when the gain is unity. The gain margin

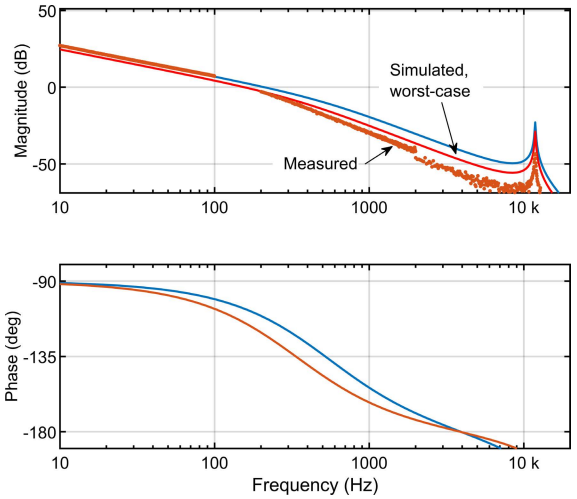

FIGURE 11. Simulated and measured loop gains of the prototype FPI controller. The blue and red curves represent worst-case values for piezo amplifier transistors, for a small and a large mirror gap. The peaks at 11 kHz are due to the mechanical resonances of the FPI.

is defined as the amount of gain increase required to make the open-loop gain unity at the frequency where the phase angle is –180°, and the modulus margin, M_M, as the minimum distance from the critical point –1 to the open-loop transfer function. It is expressed in units of dB as

$$M_M = \max_{\omega} \left(-20 \log_{10} |1 + L(j\omega)| \right), \tag{13}$$

where $L(j\omega)$ is the loop gain at angular frequency ω, i.e., the product of the gains of the blocks in the loop, Fig. 10. The "critical point –1" refers to the point $(-1+0j)$ in the Nyquist plot, in which the real and imaginary parts of the loop transfer function are plotted for all relevant frequencies.

The loop margins, simulated for the prototype, are presented in Table 2. As a general requirement for a single-input, single-output system, the Handbook recommends the following minimum values: phase margin >30°, gain margin >6 dB, and modulus margin <6 dB [14]. The minimum modulus margin is obtained in the frequency range of 1900 to 2600 Hz.

The margins are large. However, increasing the gain for faster settling would require a notch filter to attenuate the gain peak at the FPI resonance. The frequency of the dominant resonance increases with increasing gas pressure between the mirrors. The resonance in vacuum at 11 kHz shifts to 17 kHz when the FPI is used in nitrogen at atmospheric pressure. A notch filter for both these conditions would increase the complexity of the circuitry.

V. MEASUREMENT RESULTS

A. NOISE

The electronics constituting the gap controller add noise to the voltages fed to the piezo actuators. This fluctuating voltage causes the FPI mirror distance to vary, which widens and lowers the apparent spectral transmission peaks of the interferometer. For the noise assessment, the control loop was divided into sections, and the noise contribution of each block

TABLE 2. Phase, gain, and modulus margins of the FPI control loop.

Conditions	Phase margin (°)	Gain margin (dB)	Modulus margin (dB)
h_{FE} = 40, large gap	64°	47 dB	2.1 dB
h_{FE} = 250, small gap	68°	41 dB	1.9 dB

was estimated. Then, each section's noise spectral density and transfer function were used in a Simulink model to assess the effect on the gap. The noise sources were considered independent. The electronics were simulated using the simulation program LTspice, while measurements were carried out on the prototype using an HP 89410A vector signal analyzer.

The control loop model shown in Fig. 10 was used to assess the weight of the individual noise sources. The blocks are considered linear and time-invariant, each with its noise source and transfer function. The capacitance bridge and the piezo actuator were assumed to be noiseless.

1) REFERENCE AND SETPOINT VOLTAGE GENERATION

The noise of the low-pass filtered PWM signal fed to the pulse-amplitude modulator (PAM) switches acts directly as a fluctuation of the setpoint, Fig. 7. Components contributing to the noise include the voltage regulator feeding the PWM switches and the operational amplifier buffer. The supply voltage for the PWM switches is common to all switches, the reference switch and the setpoint switches. The PWM low-pass filters attenuate the noise on the supply voltage line.

The noise of the reference and setpoint signals is fed via the capacitance bridge to the preamplifier and further via the error amplifier to the demodulator. Because of the function of the modulator switches, either the reference or the setpoint voltage is fed to the bridge at any moment while the other arm is connected to ground. The capacitance bridge acts as a voltage divider for the noise, attenuating the noise of the excitation voltages by a factor of 1.5 to 3 at the preamplifier input.

2) PREAMPLIFIER

With both arms of the capacitance bridge grounded, the simulated noise spectral density at the output of the preamplifier was 6 nV/$\sqrt{\text{Hz}}$; this was not verified, as the noise floor of the analyzer was 8 nV/$\sqrt{\text{Hz}}$.

The noise of the preamplifier supply voltage, modified by the corresponding transfer function, is also present at the output. The noise spectral density of the preamplifier supply voltage peaked almost at the carrier frequency of 29 kHz. This is because the load impedance of the voltage regulator for the preamplifier was sub-optimal. A different output capacitance, or an additional low-pass filter, is needed to lower the noise density at the carrier frequency. In the prototype preamplifier, the signal attenuation from the supply voltage to the output, that is, the power supply rejection, was approximately 25 dB at the carrier frequency. This poor attenuation resulted in a

noise level at the preamplifier's output that exceeded that of the amplifier itself and the noise of the bridge excitation.

Owing to the limited space for components on the prototype preamplifier circuit board, the amplifier was implemented as a mere buffer with a gain of −1 dB. However, even with the low gain of the preamplifier, which is often undesirable, the overall performance of this gap control system suggests that the amplifier performance is adequate.

3) ERROR AMPLIFIER, PSD, AND PI-CONTROLLER

The error signal generated by the capacitance bridge and buffered by the preamplifier is amplified by the error amplifier and demodulated. The error amplifier has a band-pass frequency response centered at the carrier frequency. The maximum gain is 37 dB, decreasing by 40 dB/dec at low and high frequencies.

The PSD shifts down the error signal from 29 kHz to the frequency of the gap variations. This is the same method used for simple lock-in amplifiers. After the detector, the noise spectral density at the baseband, i.e., 0 to 1 kHz, is directly proportional to the noise density of the error signal at the carrier frequency. Thus, the high noise density of the preamplifier output signal at low frequencies is irrelevant.

An LTspice simulation of the input-referred noise of the PI-controller gives a noise voltage density of 50 nV/$\sqrt{\text{Hz}}$ up to 200 Hz, increasing by 20 dB/dec and leveling off at 200 kHz.

4) SUMMARY OF NOISE CONTRIBUTIONS

Fig. 12 shows the result of a time-domain simulation of the contributions of the dominant noise sources. The noise spectral density of each block is referred to the piezo actuator terminals. The noise on the supply voltage of the preamplifiers dominates the noise at the piezo actuators.

5) MEASURED GAP NOISE

The fluctuations in the FPI gap were estimated using the measurement setup shown in Fig. 13. The FPI was irradiated by an ultraviolet LED (Thorlabs M340L4) followed by a plano-convex lens (f = 80 mm) to collimate the light beam. Next, the radiation was filtered using a band-pass filter (Thorlabs FB340-10). Together, these produce a spectral peak with a maximum at 343 nm and a full-width-at-half-maximum of 4 nm. The central part of the radiation passing through the FPI falls on a silicon photodiode (Hamamatsu S1226-44BQ).

The photodiode signal was amplified and fed to an HP 89410A signal analyzer, together with the AC-coupled voltage across one of the piezo actuators of the FPI. Next, the gap of the FPI was adjusted to position the slope of a transmission peak on the filtered emission peak of the LED. The intensity of the light transmitted through the FPI is then a function of the FPI gap. A photodiode signal that is approximately 50% of the maximum yields the highest linearity.

The gap variation was estimated by varying the setpoint of the gap controller over several orders of interference for the 343 nm light beam. The ratio between the gap and setpoint changes was obtained using this relationship. Similarly, the relationship between the gap change and the photodiode signal was determined by varying the setpoint at the edge of the peak. With the setup used in this measurement, a gap variation of 5.8 nm gave a photodiode signal of 1 V. These values provided the scaling factor to convert the photodiode noise signal back to gap fluctuation.

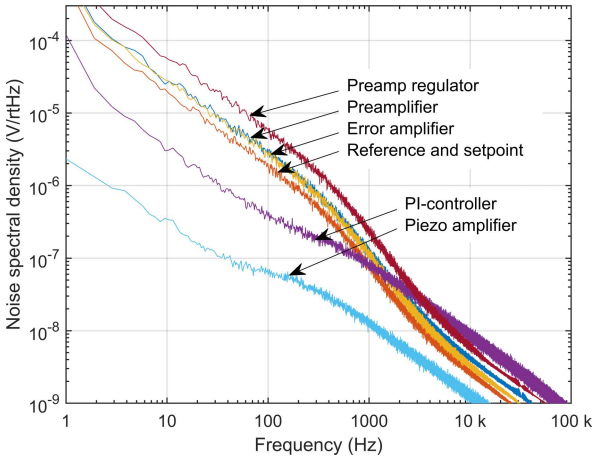

FIGURE 12. Simulated noise spectral density contributions at one piezo actuator of the FPI. The curves represent the output voltage noise spectral density of each block modified by the transfer functions of the following blocks up to the piezo actuator. The effect of the output resistance of the piezo amplifier, 1 kΩ, feeding the capacitive load of the piezo actuator, 390 nF, introduces a pole at 400 Hz.

At frequencies between 1 Hz and 20 kHz, the noise spectral density of the dark signal of the photodiode was 5 μV/$\sqrt{\text{Hz}}$. This value translates to a spectral density of gap fluctuation of 0.03 pm/$\sqrt{\text{Hz}}$ and represents the noise floor of the measurement. Gap fluctuations below this level could not be resolved.

The spectral density of the gap fluctuation, calculated from the photodiode signal, is shown in Fig. 14. The noise spectral density of the voltage across one of the piezo actuators is included for comparison.

The spectral density of the gap fluctuation is ca 0.1 pm/$\sqrt{\text{Hz}}$ at up to 200 Hz. In the band 1 Hz to 16 kHz, the total integrated photodiode noise voltage corresponds to a gap fluctuation of 4.3 pm, or 1.5 ppm for a 3 μm electrode distance.

The photodiode signal and the simulated fluctuation represent the situation in the middle of the FPI, whereas the voltage noise is measured across one piezo actuator.

Artifacts related to the 50 Hz mains frequency are visible in the photodiode and piezo voltage spectra. This was caused by an insufficiently shielded summing amplifier used for test signal injection for frequency response measurements. The peak at 130 Hz was generated by vibrations from the vacuum pump, whereas the DC/DC-converter for the piezo amplifier was responsible for the tones at 9, 1050, and 2100 Hz. The peak at 30 Hz was of unknown origin.

B. TEMPERATURE DEPENDENCE

A requirement for stable operation of the gap controller is that the ratio between the reference and setpoint voltages is

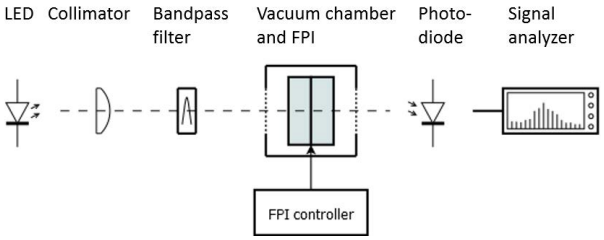

FIGURE 13. Setup for FPI gap fluctuation measurement. Gap fluctuations cause light intensity variations on the photodiode. The spectrum of the photocurrent is recorded.

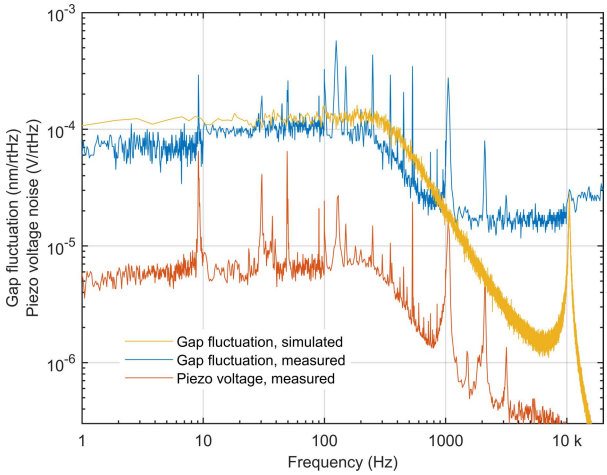

FIGURE 14. Simulated and measured gap fluctuation spectral densities and piezo voltage noise spectral density (lower curve).

unaffected by the temperature of the electronics. Therefore, the gap controller was placed in a thermal chamber to measure these voltages.

The reference and the three setpoint voltages were measured using an HP 3458A multimeter, with the signals multiplexed by an HP 34970A switch unit.

Fig. 15 shows the difference between the measured and the nominal voltage ratios, calculated as

$$\left(\left(V_{\mathrm{sp}}/V_{\mathrm{ref}}\right)/\left(N_{\mathrm{sp}}/N_{\mathrm{ref}}\right)\right) - 1, \tag{14}$$

where V_{sp} and V_{ref} are the measured setpoint and reference voltages, and N_{sp} and N_{ref} are the corresponding PWM counter commands. The errors are presented as parts per million in the temperature range of –45 to 55 °C. A change of one least significant bit of the 16-bit PWM control value corresponds to an error of 20 ppm.

In order to measure the temperature effect on the entire controller electronics, the controller was again placed in a thermal chamber. The temperature varied between –50 and 50 °C. Then, an FPI connected to the controller was placed in another thermal chamber stabilized at 30 °C.

This arrangement made it possible to focus on the gap controller and minimize any temperature effects caused by the FPI. The FPI was irradiated by a xenon light source (Thorlabs SLS401) via a fiber bundle. Another fiber led the radiation exiting the FPI to a spectrometer (Ocean Optics HR4000). The spectral centroid was calculated from the spectrometer data with the FPI set for transmission peaks at

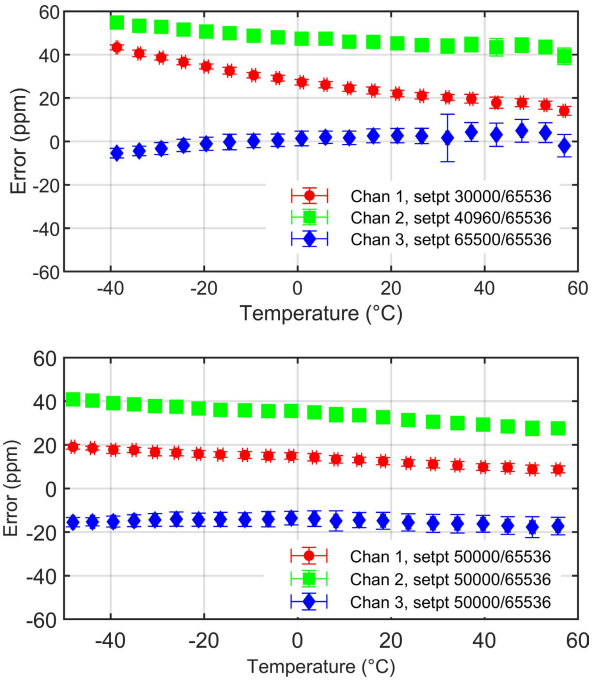

FIGURE 15. Difference between the measured and the nominal ratio between setpoint and reference voltages as a function of controller temperature. In the upper panel, the setpoints for the three channels are 30000/65536, 40960/65536, and 65500/65536. In the lower panel, the setpoint of all channels is 50000. The PWM duty cycle of the reference signal is 40960/65536 in both cases.

wavelengths of 281 or 278 nm. The former was obtained with an electrode gap of 2060 nm and the latter at 2750 nm. The corresponding orders of interference were four and nine. The gap controller setpoints were 38200 and 51000, respectively, and the reference duty cycle was 40960/65536.

In this measurement, Fig. 16, the centroid of the transmission wavelength peaks varied by less than 0.02 nm over the temperature range. A transmission wavelength shift of $\Delta\lambda$ corresponds to a gap change of $\Delta d = \Delta\lambda\, N/2$ at an order of interference of N. Thus, the gap changes were 0.04 nm at the smaller gap and 0.09 nm at the larger one. With electrode gaps of 2060 and 2750 nm, the relative electrode gap changes were 19 and 33 ppm, respectively. Related to the change in temperature, the latter corresponds to a temperature-induced drift of 0.33 ppm/°C.

C. STEP RESPONSE

An FPI-based spectral imager acquires a spectral data cube by taking a series of snapshots with the wavelength changed for each exposure. For the FPI used in this work, the wavelength of the spectral centroid must settle to within 0.05 nm of its final value in less than 50 ms after updating the controller setpoints.

Fig. 17 shows the results of four step response measurements. The initial gap was approximately 340 nm at time zero and the step sizes were 170, 340, 850, and 1530 nm. Data were collected through a stroboscopic measurement, in which a xenon flash lamp (Hamamatsu L6604) irradiated the FPI, and the transmitted light was directed to a spectrometer

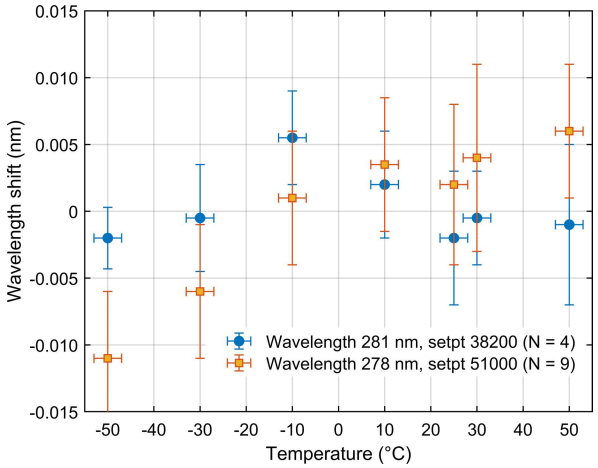

FIGURE 16. Change of FPI transmission wavelength for two gaps while the controller temperature is varied between –50 and 50 °C. Blue circles represent the deviation from the nominal wavelength of 281 nm at order N = 4, and the brown squares a wavelength of 278 nm at N = 9. The half-height of the error bars corresponds to the standard deviation of the measurements.

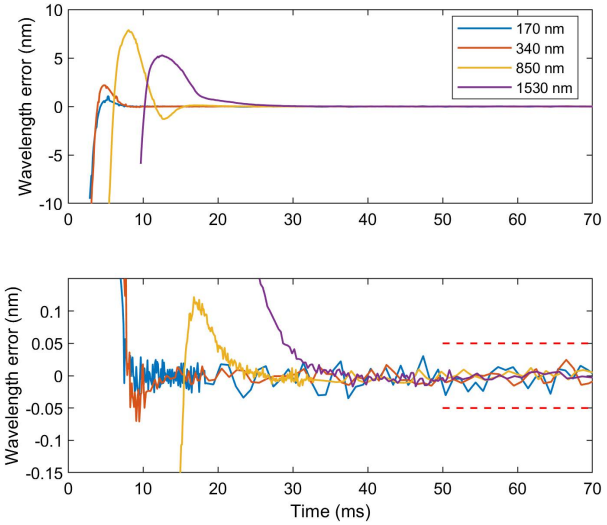

FIGURE 17. An example of settling to a commanded transmission wavelength of 340 nm for gap increments of 170, 340, 850, and 1530 nm. The initial gap was approximately 340 nm in all cases. Both panels show the same data, the lower one with a zoomed-in wavelength axis.

(Ocean Optics HR4000). The rising edge of the gap command triggered the flash lamp after an adjustable delay. Settling is presented in terms of the wavelength error, which is the difference between the measured centroid wavelength of the relevant transmission peak and the final steady state wavelength. The FPI was installed in a rough vacuum, and the gap was alternated at a rate of 0.2 Hz.

The transmission peaks are broader at low orders of interference (170 and 340 nm steps), and the noise of the centroid measurement is correspondingly higher at these mirror gaps.

The 850 and 1530 nm steps cause large error signals that saturate the signal chain. Saturation causes noticeably slower settling after large steps.

D. IMPACT OF CLOCK FREQUENCY VARIATION

The crystal oscillator driving the main FPGA controls the timing of all switching actions. By replacing the crystal oscillator with a signal generator, the clock frequency was changed between 70% and 130% of the nominal frequency while measuring its effect on the FPI transmission wavelength. The ratio of the relative change in the electrode gap to the relative frequency change was $(\Delta d_{\mathrm{ele}}/d_{\mathrm{ele}})/(\Delta f_{\mathrm{osc}}/f_{\mathrm{osc}}) = 0.6{\cdot}10^{-3}$. A crystal oscillator typically exhibits a relative frequency drift of less than 100 ppm over its operating temperature range. For example, with an electrode gap of 3 μm, the resulting gap change would be 0.2 pm or less than 0.1 ppm. Thus, the effect of clock frequency drift is negligible.

VI. DISCUSSION

The FPI controller presented in this work is characterized by

- Nulling capacitive measurement bridges, easing the requirements for the gain stability of the following amplifier stages,
- Excitation of the bridges by square wave voltages with adjustable amplitude,
- PWM-based digital-to-analog conversion for an accurately determined ratio of the excitation voltages, and
- No transformer in the signal path, reducing the cost of procurement of space-qualified components.

TABLE 3. FPI controller performance comparison.

FPI Controller	Temperature drift (ppm/°C)	Gap noise (ppm rms)	Noise spectral density (ppm/√Hz)	Ref.
ADS100		48		[5]
CS100	<1		<0.2	[15]
E-509	<30		0.115	[16]
MALICE	4	9.4		[17]
This work	0.3	1.5	0.04	

The FPI controller generated a temperature-induced variation in the FPI gap of less than 0.025 nm over the temperature range of –50 to 50 °C and a gap fluctuation of less than 5 pm in the frequency range of 1 Hz to 16 kHz. These values translate to 30 ppm and 2 ppm, respectively, expressed as relative variations in the electrode gap. The measured performance satisfied the design requirement for a gap variation of less than 0.1 nm. Although the measurements were made on only a couple of gap controllers, the concept and circuit solutions are believed to be robust, sound, and suitable for further usage in engineering and flight models.

Table 3 compares the temperature-induced drift and the noise of FPI controllers described in the literature to those of the controller designed in this study. As the electrode gaps of the measurement capacitors were different, the reported drift and noise values were normalized to the electrode gap used.

The ADS100 is a digital FPI controller developed at the University of Rome Tor Vergata [5]. The CS100, manufactured by IC Optical Systems Ltd, is used in many ground-based solar and astronomical telescopes [15]. The position control module E-509, made by Physik Instrumente [16], has been used to develop advanced control algorithms for FPIs. MALICE, built by COM DEV Ltd, is based on the

controller planned for the Tunable Filter Imager on the James Webb Space Telescope [17]. The measurement conditions giving the values in Table 3 are not reported in detail; this must be kept in mind when comparing the controllers. The values for temperature-induced drift exclude the FPI, and only the contribution of the controller is considered.

VII. CONCLUSION

This paper describes the implementation of a space-grade controller for a Fabry-Perot interferometer. The controller is based on capacitive sensing of the distance between the mirrors of a piezo-electrically actuated FPI. The controller is designed for the ultra-violet channel of the ALTIUS spectral imager comprising a cascade of four FPIs.

The controller electronics are based on components available with the quality level required for a satellite instrument. The concept is based on a novel combination of square wave excitation of the capacitance bridge used to measure the FPI mirror gap and the generation of these signals by fractional-N-based pulse-width modulators. Using identical circuits for the reference and setpoint signals, this method generates stable ratios between these voltages, and therefore, high immunity to temperature variations.

According to measurements made on prototype controllers, the performance met the prime requirements for temperature-induced drift and fluctuations of the FPI mirror gap caused by electronic noise.

Based on a comparison with four FPI controllers reported in the literature, the controller implemented in this work demonstrates the best stability performance in terms of temperature-induced drift and controller-generated FPI mirror gap fluctuation.

REFERENCES

[1] D. Fussen, N. Baker, J. Debosscher, E. Dekemper, P. Demoulin, Q. Errera, G. Franssens, N. Mateshvili, N. Pereira, D. Pieroux, and F. Vanhellemont, "The ALTIUS atmospheric limb sounder," *J. Quant. Spectrosc. Radiat. Transf.*, vol. 238, Nov. 2019, Art. no. 106542, doi: 10.1016/j.jqsrt.2019.06.021.

[2] L. Montrone, L. Aballea, D. Bernaerts, D. Navarro-Reyes, S. Santandrea, N. Saillen, K. Sarna, P. Holbrouck, W. Moelans, D. Kendall, D. Mollet, R. De Nutte, S. Demidov, H. Saari, J. Ward, R. Kassel, D. Fussen, E. Dekemper, E. Neefs, and J. Vanhamel, "Technological innovation for the ALTIUS atmospheric limb sounding mission," *Proc. SPIE*, vol. 11151, pp. 114–133, Oct. 2019, doi: 10.1117/12.2533151.

[3] E. Hecht, "Interference," in *Optics*, vol. 1, 4th ed. San Francisco, CA, USA: Pearson, 2002, p. 421, ch. 9, sec. 9.6.

[4] T. R. Hicks, N. K. Reay, and P. D. Atherton, "The application of capacitance micrometry to the control of Fabry–Perot etalons," *J. Phys. E, Sci. Instrum.*, vol. 17, no. 1, pp. 49–55, Jan. 1984, doi: 10.1088/0022-3735/17/1/010.

[5] L. Giovannelli, F. Berrilli, D. Del Moro, D. Gallieni, G. Martiniello, and P. Fumi, "Digital controller for capacitance stabilized etalons," in *Proc. IEEE Int. Conf. Wireless Space Extreme Environ. (WiSEE)*, Vicenza, Italy, Oct. 2020, pp. 66–71, doi: 10.1109/WiSEE44079.2020.9262662.

[6] R. Mannila, A. Näsilä, K. Viherkanto, C. Holmlund, I. Näkki, and H. Saari, "Spectral imager based on Fabry–Perot interferometer for Aalto-1nanosatellite," *Proc. SPIE*, vol. 8870, Sep. 2013, Art. no. 887002, doi: 10.1117/12.2023299.

[7] A. Näsilä, C. Holmlund, R. Mannila, I. Näkki, H. J. Ojanen, A. Akujärvi, H. Saari, D. Fussen, D. Pieroux, and P. Demoulin, "PICASSO VISION instrument design, engineering model test results, and flight model development status," *Proc. SPIE*, vol. 10001, pp. 50–63, Oct. 2016, doi: 10.1117/12.2241956.

[8] I. Ouattara, J.-L. Gach, and P. Amram, "A new driving method for piezo deformable mirrors: Open loop control and MOAO made easy," *Proc. SPIE*, vol. 9909, pp. 228–235, Jul. 2016, doi: 10.1117/12.2231684.

[9] Z. Li, J. Shan, and U. Gabbert, "Dynamics modeling and inversion-based synchronized model predictive control for a Fabry–Perot spectrometer," *IEEE/ASME Trans. Mechatronics*, vol. 24, no. 4, pp. 1818–1828, Jul. 2019, doi: 10.1109/TMECH.2019.2927752.

[10] Z. Li and J. Shan, "Modeling and inverse compensation for coupled hysteresis in piezo-actuated Fabry–Perot spectrometer," *IEEE/ASME Trans. Mechatronics*, vol. 22, no. 4, pp. 1903–1913, Aug. 2017, doi: 10.1109/TMECH.2017.2703167.

[11] T. R. Hicks and P. D. Atherton, "Capacitance sensors," in *The Nanopositioning Book*. Berkshire, U.K.: Queensgate Instruments Ltd, 1997, p. 68.

[12] (2021). *ESCC Qualified Parts List (QPL), ESCC/RP/QPL005–219 (REP 005)*. European Space Components Coordination. [Online]. Available: https://escies.org/download/downloadRep005

[13] D. P. Blair and P. H. Sydenham, "Phase sensitive detection as a means to recover signals buried in noise," *J. Phys. E, Sci. Instrum.*, vol. 8, no. 8, pp. 621–627, Aug. 1975, doi: 10.1088/0022-3735/8/8/001.

[14] (Dec. 2010). Space engineering. *Control Performance Guidelines, ECSS-E-HB-60–10A, European Cooperation for Space Standardization*. [Online]. Available: https://ecss.nl/hbstms/ecss-e-hb-60-10a-control-performance-guidelines/

[15] IC Optical System Ltd. Beckenham, U.K. *CS100 Closed Loop Controller*. Accessed: Feb. 15, 2022. [Online]. Available: https://www.icopticalsystems.com/?page_id=70

[16] Physik Instrumente GmbH. Karlsruhe, Germany. *Signal Conditioner/Piezo Servo Module E-509*. Accessed: Feb. 15, 2022. [Online]. Available: https://static.physikinstrumente.com/fileadmin/user_upload/physik_instrumente/files/datasheets/E-509-Datasheet.pdf

[17] A. Scott, M. Javed, R. Abraham, S. Eikenberry, E. Barton, M. Bershady, J. Bland-Hawthorn, D. Crampton, R. Doyon, J. Julian, R. Julian, J.-P. Kneib, D. Loop, N. Raines, N. Rowlands, and J. D. Smith, "Performance of F2T2 tandem tunable etalon," *Proc. SPIE*, vol. 6269, pp. 1768–1777, Jun. 2006, doi: 10.1117/12.668774.

CHRISTER HOLMLUND (Member, IEEE) received the master's degree in applied electronics and the Lic.Tech. degree in measurement technology from the Helsinki University of Technology, Espoo, Finland, in 1983 and 1990, respectively. He is currently a Senior Scientist with the VTT Technical Research Centre of Finland, Espoo. His research interests include electronics and firmware design of microspectrometers and hyperspectral imagers.

ROBERTS TROPS received the B.Sc.Eng. and M.Sc.Eng. degrees in electronics engineering from the Ventspils University of Applied Sciences, in 2013 and 2015, respectively. He is currently pursuing the Ph.D. degree with Aalto University, specializing in space science and technologies. He is also a Research Scientist with the VTT Technical Research Centre of Finland. His research interests include programming, PCB design, and embedded system design. He specializes in development of hyperspectral imaging devices.